



**HAL**  
open science

## Colloidal Nanocube Supercrystals Stabilized by Multipolar Coulombic Coupling

Henry Chan, Arnaud Demortière, Lela Vukovic, Petr Král, Petit Christophe

► **To cite this version:**

Henry Chan, Arnaud Demortière, Lela Vukovic, Petr Král, Petit Christophe. Colloidal Nanocube Supercrystals Stabilized by Multipolar Coulombic Coupling. ACS Nano, 2012, 6 (5), pp.4203-4213. 10.1021/nm3007338 . hal-01978620

**HAL Id: hal-01978620**

**<https://hal.sorbonne-universite.fr/hal-01978620>**

Submitted on 11 Jan 2019

**HAL** is a multi-disciplinary open access archive for the deposit and dissemination of scientific research documents, whether they are published or not. The documents may come from teaching and research institutions in France or abroad, or from public or private research centers.

L'archive ouverte pluridisciplinaire **HAL**, est destinée au dépôt et à la diffusion de documents scientifiques de niveau recherche, publiés ou non, émanant des établissements d'enseignement et de recherche français ou étrangers, des laboratoires publics ou privés.

## Colloidal Nanocube Supercrystals Stabilized by Multipolar Coulombic Coupling

Henry Chan, Arnaud Demortiere, Lela Vukovic, Petr Kral, and Christophe Petit

ACS Nano, Just Accepted Manuscript • DOI: 10.1021/nn3007338 • Publication Date (Web): 15 Apr 2012

Downloaded from <http://pubs.acs.org> on April 24, 2012

### Just Accepted

“Just Accepted” manuscripts have been peer-reviewed and accepted for publication. They are posted online prior to technical editing, formatting for publication and author proofing. The American Chemical Society provides “Just Accepted” as a free service to the research community to expedite the dissemination of scientific material as soon as possible after acceptance. “Just Accepted” manuscripts appear in full in PDF format accompanied by an HTML abstract. “Just Accepted” manuscripts have been fully peer reviewed, but should not be considered the official version of record. They are accessible to all readers and citable by the Digital Object Identifier (DOI®). “Just Accepted” is an optional service offered to authors. Therefore, the “Just Accepted” Web site may not include all articles that will be published in the journal. After a manuscript is technically edited and formatted, it will be removed from the “Just Accepted” Web site and published as an ASAP article. Note that technical editing may introduce minor changes to the manuscript text and/or graphics which could affect content, and all legal disclaimers and ethical guidelines that apply to the journal pertain. ACS cannot be held responsible for errors or consequences arising from the use of information contained in these “Just Accepted” manuscripts.



# Colloidal Nanocube Supercrystals Stabilized by Multipolar Coulombic Coupling

Henry Chan<sup>1</sup>, Arnaud Demortière<sup>2,3</sup>, Lela Vuković<sup>1</sup>, Petr Král<sup>1,4</sup>, and Christophe Petit<sup>2</sup>

<sup>1</sup> *Department of Chemistry, University of Illinois at Chicago, Chicago, IL 60607, USA*

<sup>2</sup> *Laboratoire des Matériaux Mésostructurés et Nanométriques,*

*Université Pierre et Marie Curie - CNRS (UMR 7070),*

*4 place Jussieu 75252 Paris Cedex 05, France*

<sup>3</sup> *Center for Nanoscale Materials, Argonne National Laboratory,*

*9700 S. Cass Ave., Argonne, IL 60439, USA and*

<sup>4</sup> *Department of Physics, University of Illinois at Chicago, Chicago, IL 60607, USA*

(Dated: April 15, 2012)

## Abstract

We explore microscopic principles governing the self-assembly of colloidal octylamine-coated platinum nanocubes solvated in toluene. Our experiments show that regular nanocubes with the edge length of  $l_{RC} = 5.5$  nm form supercrystals with the simple cubic packing, while slightly truncated nanocubes with the edge length of  $l_{TC} = 4.7$  nm tend to arrange in the *fcc* packing. We model by averaged force fields and atomistic molecular dynamics simulations the coupling forces between these nanocrystals. Our detailed analysis shows that the *fcc* packing, which for cubes has a lower density than the simple cubic packing, is favored by the truncated nanocubes due to their Coulombic coupling by multipolar electrostatic fields, formed during a charge transfer between the octylamine ligands and the Pt cores.

**Keywords:** molecular dynamics, self-assembly, nanocubes, multipolar coupling, charge transfer

E-mail: pkral@uic.edu, ademortiere@anl.gov

1  
2  
3  
4 In recent years, colloidal nanoparticles (NP) of different materials,<sup>1-4</sup> sizes,<sup>5</sup> shapes,<sup>6-16</sup>  
5 and coatings<sup>17-20</sup> have been self-assembled into superlattices with many types of packing.<sup>21-23</sup>  
6 It is crucial to understand microscopic principles governing the processes of NP self-  
7 assembly<sup>24</sup> in order to control structural,<sup>25</sup> chemical,<sup>26,27</sup> and physical properties of the  
8 formed superlattices.<sup>28,29</sup> These novel metamaterials may exhibit new functionalities when  
9 applied in electronics,<sup>30</sup> optics,<sup>31,32</sup> magnetism,<sup>33</sup> and catalysis.<sup>34,35</sup>

14 In most cases, the self-assembly of colloidal NPs is thermodynamically driven by inter-  
15 particle forces determined by the NP type,<sup>36</sup> the solvent type,<sup>37</sup> and other conditions  
16 used during the evaporation processes.<sup>38-40</sup> Typically, NPs interact with each other and  
17 the substrate<sup>41</sup> by van der Waals (vdW), steric, and Coulombic coupling,<sup>42-44</sup> originating  
18 from the NP bulks and ligands.<sup>17,45</sup> The related forces can be obtained in atomistic<sup>46</sup> or  
19 coarse-grained modeling<sup>47</sup> and approximated by averaged force-fields acting between the  
20 NPs.<sup>38,42,43,48-51</sup>

25 Spherical colloidal NPs with isotropic inter-particle coupling tend to self-assemble into  
26 closed-packed *fcc* and *hcp* structures.<sup>52</sup> Anisotropic forces between the NPs, such as those  
27 originating in electric/magnetic dipole-dipole coupling, can lead to simple hexagonal (*sh*) or  
28 body-centered cubic (*bcc*) structures.<sup>42,43</sup> Nonspherical particles can have a large range of  
29 packing densities, common interfaces between crystalline facets, and intriguing geometries  
30 of void spaces, which can drastically influence the superlattice properties.<sup>53</sup> For example,  
31 polyhedral nanocrystals may self-organize into more open superlattices, such as cubic and  
32 octahedral nanocrystals.<sup>10-16,54</sup> Even though many types of superstructures have been pre-  
33 pared, the principles that control their self-assembly are not well understood.<sup>16</sup>

36 In this work, we combine experimental and theoretical efforts to investigate the packing  
37 principles in supercrystals formed of regular (RC) and truncated (TC) colloidal platinum  
38 nanocubes (NC). We model with averaged force fields and atomistic molecular dynamics  
39 simulations the vdW and Coulombic coupling forces between RCs and TCs to explain their  
40 observed self-assembly in supercrystals with simple cubic (*sc*) and *fcc* packings, respectively.  
41 After careful analysis, we conclude that the looser *fcc* packing of TCs originates in their  
42 multipolar Coulombic coupling, where a charge is passed to the TCs from their ligands and  
43 asymmetrically redistributed in their metallic cores.

#### 54 **Observed NC supercrystals**

56 We have prepared RCs and TCs coated with octylamine and solvated in toluene,<sup>55</sup> using

1  
2  
3  
4 a liquid-liquid phase transfer method.<sup>13,56</sup> The average edge lengths (between two opposite  
5 {100} faces) of the NCs are  $l_{RC} = 5.5$  nm and  $l_{TC} = 4.7$  nm, with the size distribution of  
6 8% and 9%, respectively. In the insets of Fig. 1 (c) (left and right), we show TEM images of  
7 the {100} faces of the RC and TC, where the TC has {111} facets on its truncated corners.  
8  
9 In our experiments, we observe that the prepared RCs form simple cubic superlattices and  
10 the TCs form *fcc* superlattices. The *sc* structures are rare in Nature, but they have been  
11 observed in Po crystals<sup>57</sup> and TiO<sub>2</sub>-P<sub>2</sub>O<sub>5</sub> NC supercrystals.<sup>58</sup>

12  
13  
14 In Fig. 1 (a) and (c), we use TEM to show the stacking pattern of 2 – 4 NC layers of RCs  
15 (left) and TCs (right) lattices, where the white squares denote their primitive cells. The two  
16 types of superlattices are schematically shown in Fig. 1 (b), where the RCs are positioned  
17 in the face-to-face (*f – f*) configuration (*sc* lattice) and the TCs are in the shifted corner-  
18 to-corner (*c – c*) configuration (*fcc* lattice). Sequential RC layers are stacked on the top  
19 of each other (labeled as AAA), whereas each TC layer (considered along the diagonal of  
20 the *fcc* cube in the inset of Fig. 5 (b)) is stacked at the interstitial sites of the next layer  
21 (ABCABC), such that each successive layer is shifted by half the repetition distance. The  
22 lattice constants obtained from TEM,  $a_{sc} \approx 7$  nm and  $a_{fcc} \approx 11$  nm, are in good agreement  
23 with those,  $A_{sc} \approx 8$  nm and  $A_{fcc} \approx 11$  nm, measured by the selected area electron diffraction  
24 (SAED) at 250 cm.

25  
26  
27 Recently, Yamamuro *et al.* have evaluated the vdW (ligand) coupling of model NCs in  
28 different 3D<sup>51</sup> and 2D stacking.<sup>59</sup> Their results show that the face-to-face assembly in the  
29 *sc* structure has the lowest potential energy. Our experiments also show that RCs form *sc*  
30 superlattices, but it is not clear why TCs with small corner truncations form the loose *fcc*  
31 superlattices. We model the NCs to understand how small changes in their shapes can lead  
32 to remarkably different superstructures.

33  
34  
35 In Fig. 2 (a), we present SEM images of RCs forming *sc* supercrystals (lateral size of  
36 0.5 – 2.0  $\mu\text{m}$ ), which are rarely formed on the substrate (inset) and often stacked in a  
37 random manner. The high-resolution SEM-FEG images in Fig. 2 (b) clearly show that a  
38 supercrystal can have a long-range order at the length scale of  $\approx 1$   $\mu\text{m}$ . The face of the  
39 supercrystal is a {100}<sub>sp</sub> (sp=superlattice) surface (inset Fig. 2 (b)). The magnified SEM-  
40 FEG image reveals stacking faults in the cubic arrangement, which are likely due to local  
41 inhomogeneity of NC shapes or local perturbations formed during the growth process.

42  
43  
44 Figure 3 (a–d) shows SEM images of TCs forming *fcc* supercrystals. On the substrate,

1  
2  
3  
4 supercrystals with a low polydispersity and two types of morphologies are seen to form:  
5 square pyramids (Fig. 3 (a–b)) and triangular prisms (Fig. 3 (c–d)). The  $[100]_{sp}$  axis of  
6 pyramidal crystals and the  $[111]_{sp}$  axis of triangular crystals are normal to the substrate.  
7 From the SAED images of a sample at  $30^\circ$  tilt,<sup>13</sup> we determined the angle between the  
8 substrate and the faces of the pyramidal crystals to be  $\approx 45^\circ$ . The size of the pyramids is  
9  $\approx 12 \mu\text{m}$ , with the size distribution of 20%, and the size of the triangles is  $\approx 9 \mu\text{m}$ , with  
10 the size distribution of 30%.

11  
12  
13  
14  
15 In rare cases, we observe TC supercrystals with other morphologies. In Fig. 4 (a–c), we  
16 show SEM images of hexagonal, quasi-hexagonal, and triangular supercrystals. The multi-  
17 layer textured surfaces on the faces of these supercrystals indicate that the supercrystals  
18 have similar growth processes but different growth times. In Fig. 4 (d–f), we show SEM im-  
19 ages of elongated, cleaved (crushed) with a well defined internal structure, and decahedron  
20 supercrystals; the five-fold symmetry could be due to multiple twinning.<sup>60</sup> These supercrystal-  
21 ls are likely formed due to the presence of faults in the *fcc* stacking or the emergence of  
22 other growth axes induced by particle-substrate interactions.

### 23 24 25 26 27 28 29 **Supercrystal growth**

30  
31 In order to prepare uniform supercrystals with a long-range order, shown in Figs. 2-  
32 4, slow crystallization conditions must be guaranteed. We use a glass tube to create a  
33 limited air/solution interface, which allows us to achieve a very slow evaporation rate (8  
34 days) of toluene ( $bp = 110^\circ\text{C}$ ) at  $25^\circ\text{C}$ . Our TEM specimens are prepared by immersing  
35 a carbon-coated TEM grid in the glass tube containing  $200 \mu\text{L}$  of colloidal solution with  
36 a concentration of  $2 \times 10^{-5}$  mol/L. SEM specimens are obtained by immersing a silicon  
37 substrate (Si wafer) in the glass tube containing 2 mL of the same colloidal solution. It  
38 is useful to describe the nucleation and growth of NC crystals in more detail to disclose  
39 potential principles of their self-assembly.

#### 40 41 42 43 44 45 46 *a) Supercrystal nucleation*

47  
48 The growth of supercrystals of colloidal NCs starts by the spontaneous formation of a  
49 crystalline nuclei, which takes part either homogeneously in the solution or heterogeneously  
50 on a substrate.<sup>61</sup> The energy barrier of homogeneous nucleation,  $\Delta G_N^{homo}$ , is usually larger  
51 (more limiting) than the barrier of heterogeneous nucleation,  $\Delta G_N^{hete}$ . The barriers can be  
52 affected by the strength of inter-particle interactions, the solvent evaporation rate, NC-  
53 substrate interfacial properties, and other factors.

1  
2  
3  
4 In RCs, the strong vdW interactions between their  $\{100\}$  faces may allow the *sc* super-  
5 lattice to form in solution. Once formed, the crystallites attach to the substrate, where they  
6 continue to grow, as seen in Fig. 2 (a). Their nucleation appears to be mainly homogeneous,  
7 since the supercrystals are in random positions on the substrate. Consequently, diffraction  
8 patterns reveal only homogeneous rings and the small angle x-ray diffraction (SA-XRD)  
9 pattern indicates the absence of a single-growth axis.<sup>13</sup>

10  
11  
12  
13  
14 On the other hand, the *fcc* superlattice aggregates seem to be stabilized by corner-to-  
15 corner interactions of the TCs, which might be difficult to materialize in a repetitive manner  
16 without a substrate. In Fig. 3, we seem to observe that NCs self-organize on substrates,  
17 where they grow into supercrystals with different morphologies, in dependence of the facets  
18 lying on the substrate. The initial square arrangement of the  $\{100\}_{sp}$  basic plane yields a  
19 pyramidal *fcc* crystal, whereas a hexagonal layer,  $\{111\}_{sp}$  basic plane, yields a triangular *fcc*  
20 crystal (no  $C_3$  symmetry due to NCs in the lattice points). This is confirmed by previous  
21 SA-XRD observations, which reveal the  $[001]_{sp}$  growth axis (perpendicular to the substrate)  
22 for the pyramidal supercrystals and the  $[111]_{sp}$  growth axis for the triangular supercrystals.<sup>13</sup>

#### 23 24 25 26 27 28 29 *b) Deliberation of the NC coupling forces*

30  
31 In order to understand what drives the self-assembly in the observed RCs and TCs super-  
32 structures, we will try to characterize the dominant forces between the NCs. Although the  
33 observed superlattices are probably nucleated in the colloidal phase (solution or substrate),  
34 they can be further stabilized during the solvent evaporation. We can estimate these pro-  
35 cesses from the NC-binding Gibbs free energy,  $\Delta G = \Delta H - T\Delta S$ , in *solvent* and *vacuum*.  
36 We briefly discuss the important terms involved in  $\Delta G$ .

37  
38  
39  
40 In principle, large polarizabilities of the metal NC cores result in dispersion forces that  
41 can induce the self-assembly of colloidal NPs at room temperature.<sup>38,49</sup> The strength of this  
42 bulk vdW core-core coupling,  $\Delta H_{core}^{vdW}$ , grows with the polarizabilities of the interacting NPs.  
43 The Pt NC cores are much more polarizable than the toluene solvent and the octylamine  
44 ligands on the NCs, so the strength of vdW coupling (per unit volume) ranks as core-core >  
45 core-ligand > ligand-ligand  $\approx$  ligand-solvent. When the solvent and ligands are chemically  
46 similar, we can neglect the ligand-ligand vdW coupling and consider just the core-core vdW  
47 coupling.<sup>42,43</sup> We suspect that this coupling alone can not explain the self-assembly of loose  
48 *fcc* superstructures formed by the TCs. It is also unlikely that the vdW coupling associated  
49 with the ligands (of different densities)<sup>25</sup> close to the (shifted) corners of neighboring TCs  
50  
51  
52  
53  
54  
55  
56  
57  
58  
59  
60

could create the local minima in  $\Delta G$ , which is necessary for the *fcc* lattice stabilization.

The loose *fcc* superstructures might be self-assembled by *directional forces* acting between colloidal TCs and providing the local energy minima in  $\Delta G$  around their corners. Such local minima could originate from a multipolar Coulombic coupling, caused for example by partial charge transfer between the ligands and the Pt NC-cores.<sup>62</sup> Electrons in the vicinity of the ligand binding sites (Pt atoms) can be transferred to the more electronegative octylamine ligands (N atoms). Inside the metallic NC, the charge can freely redistribute and locally charge the NC, as schematically shown in Fig. 6 (a). The (neutral) TCs can interact with each other in toluene at relatively large distances, as characterized by  $\Delta H_{NC}^{elec}$ , and direct the self-assembly of *fcc* superlattices.

Once the solvent is evaporated (vacuum), the ligand-ligand vdW coupling enthalpy,  $\Delta H_{ligand}^{vdW}$ , and the related entropy,  $\Delta S_{ligand}$ , can dominate in  $\Delta G$ . When the ligands interdigitate more, their entropy,  $\Delta S_{ligand}$ , decreases (limited space and ligand conformations), which counter-balances the growth of  $\Delta H_{ligand}^{vdW}$ . The ligand-ligand coupling might seal the superstructure pre-stabilized in solvent by the Coulombic coupling and the bulk vdW core-core coupling.

### Modeling of the NC self-assembly

In the following, we will calculate the various contributions to  $\Delta G$  to estimate which of them might activate and guide the NC self-assembly. First, we model the microscopic bulk vdW core-core coupling between NCs by average force fields. Then, we evaluate by atomistic molecular dynamics (MD) simulations the NC coupling associated with their polarized ligands and NC cores.

#### A) Microscopic modeling (bulk vdW coupling)

The (NC-core) vdW potential energy between two NCs (*i*th and *j*th) can be approximated by the Hamaker pairwise summation,<sup>43,63</sup>

$$V = V_{core}^{vdW}(ij) = -\frac{A}{\pi^2} \int_{V_i} \int_{V_j} \frac{1}{r_{ij}^6} d\vec{r}_i d\vec{r}_j. \quad (1)$$

where,  $A$  is the Hamaker constant that depends on the type of NC core and  $r_{ij}$  is the distance between atoms (microscopic elements) of the two NCs.

Due to the fast decay of the vdW coupling (the  $1/r^6$  term), we only consider interactions between the NC and its first neighbors. We obtain the vdW potential energy per NC in the



1  
2  
3  
4 *sc* superlattice,

$$5 \quad V^{sc} = \frac{1}{2} (6 V_{f-f} + 12 V_{e-e} + 8 V_{dc-dc}) , \quad (2)$$

6  
7 where the subscripts in  $V$  indicate the face-to-face ( $f - f$ ), edge-to-edge ( $e - e$ ), and direct  
8 corner-to-corner ( $dc - dc$ ) NC coupling terms (in the last term, NC corners are frontally  
9 arranged with respect to each other). Likewise, we obtain the vdW energy for the *fcc*  
10 superlattice,

$$11 \quad V^{fcc} = \frac{1}{2} (4 V_{f-f} + 4 V_{e-e} + 8 V_{c-c}) , \quad (3)$$

12  
13 where we consider the intra-layer face-to-face ( $f - f$ ), intra-layer edge-to-edge ( $e - e$ ), and  
14 inter-layer shifted corner-to-corner ( $c - c$ ) NC coupling terms (we mean horizontal layers  
15 shown in the inset of Fig. 5 (b));  $dc - dc$  is replaced by  $c - c$  because the corner facets of  
16 the TCs in the *fcc* superlattice are not aligned. In the calculations, we use the averaged  
17 experimental edge lengths (between two opposite  $\{100\}$  faces) of  $l_{RC} = 5.5$  nm and  $l_{TC} = 4.7$   
18 nm. The  $\{111\}$  corner facets of the TC are characterized by the experimental length of the  
19 corner truncation,  $\alpha = 0.85$  nm, measured along the NC edge.

20  
21 First, we calculate  $V^{sc}$  for RCs and TCs by varying the face-to-face inter-nanocube dis-  
22 tance,  $d_{sc}$ , as shown in Fig. 5 (a). The Hamaker constant for Pt-Pt coupling (through octy-  
23 lamine ligands) is approximated by its value for gold-gold coupling (through dodecanethiol),  
24  $A \approx 2$  eV.<sup>64</sup> The results show that  $V^{sc}$  is always smaller (more stable) for RCs than for TCs.  
25 The vertical line depicted in Fig. 5 (a) marks the experimentally observed inter-particle  
26 distance of RCs in the *sc* superlattice. At this distance, determined by the ligand length,  
27 we find that  $V_{RC}^{sc} = -13.1$  kcal/mol and  $V_{TC}^{sc} = -7.5$  kcal/mol. The difference is caused by  
28 different sizes of the NCs and the presence of small truncations in TCs.

29  
30 Next, we calculate  $V^{fcc}$  for RCs and TCs, by varying their intra-layer ( $a_{fcc}$ ,  $b_{fcc}$ ) and inter-  
31 layer ( $c_{fcc}$ ) distances. Since the *fcc* superlattice formed of TCs has  $C_4$  symmetry (seen in  
32 Fig. 1 (b) (right)), we consider that  $a_{fcc} = b_{fcc}$ . The NCs in the *fcc* superlattice have larger  
33 intra-layer distances than those in the *sc* superlattice, but their inter-layer distances are  
34 smaller due to the ABCABC stacking pattern. In Fig. 5 (b), we show the  $V^{fcc}$  energy contour  
35 map calculated for the TCs. The potential energy of  $V_{TC}^{fcc} = -6.7$  kcal/mol is obtained at  
36 the point  $a_{fcc} = b_{fcc} = c_{fcc} = 11$  nm. This point marks the experimentally observed shifted  
37 corner-to-corner TC configuration, where neighboring TCs have sub-nanometer (inter-layer)  
38 face-to-face distance of  $d_{fcc} = 0.8$  nm (based on  $c_{fcc} = 11$  nm and  $l_{TC} = 4.7$  nm). In Fig. 5  
39  
40  
41  
42  
43  
44  
45  
46  
47  
48  
49  
50  
51  
52  
53  
54  
55  
56  
57  
58  
59  
60

(b), we also show that neighboring TCs in the *fcc* structure do not have aligned corners. The sloped line at the bottom of the contour map marks the configurations where the corner facets of the TCs are aligned ( $a_{fcc} = b_{fcc} = \sqrt{2}c_{fcc}$ ).

The energy contour map shows that the large intra-layer distance between TCs in the *fcc* superlattice ( $a_{fcc}, b_{fcc}$ ) could be stabilized by the small inter-layer distance (included in  $c_{fcc}$ ). The fact that TCs experimentally assemble with a small (inter-layer) face-to-face distance ( $d_{fcc} = 0.8$  nm) might indicate that the ligand density is lower (less steric repulsion) on the  $\{111\}$  corner facets than on the  $\{100\}$  faces. However, it is difficult to argue why TCs in the experiment do not align their corner facets, which should give a stronger corner-to-corner coupling. The bulk vdW coupling also does not give a clear “visible” local minimum at large NC separations, which is necessary for the formation of the *fcc* structure.

## B) Atomistic modeling

The above mean-field model shows that bulk vdW forces might allow TCs to self-assemble into loose *fcc* structure, but the results do not explain the observed shift of corners and they do not provide a significant local energy minimum that would prevent the loose *fcc* structure from switching to the more compact *sc* structure. To address these issues, we use atomistic molecular dynamics (MD) simulations to model molecular forces between neighboring TCs. We assume that TCs interact through vdW coupling of their octylamine ligands and Coulombic coupling between partial charges on their ligands and cores, formed due to the charge transfer along N-Pt bonds.

### a) Model of the NCs

In Fig. 6 (a) we show our atomistic model of two TCs in the shifted corner-to-corner (*c-c*) configuration. Each TC has a Pt core protected by a monolayer of octylamine ligands, with the edge length (between two opposite  $\{100\}$  faces) of  $l_{TC} = 4.704$  nm, based on the experimental value of  $l_{TC} = 4.7$  nm. The  $\{111\}$  corner facets are characterized by the corner truncation parameter of  $\alpha = 0.784$  nm, obtained by removing 3 Pt layers; it is close to the experimental value of  $\alpha = 0.85$  nm.

In the MD simulations, we maintain the shape and rigidity of the core by Pt-Pt bonds with large bond strength of  $\approx 10^4$  kcal/mol  $\text{\AA}^2$ , added in the force field. The NC core has *fcc* packing with the lattice constant of  $a = 3.92$   $\text{\AA}$ , derived from the equilibrium Pt-Pt bond length of  $b_0 = 2.77$   $\text{\AA}$ . Each TC core has 7,758 Pt atoms, where 1,494 and 24 of them are exposed on the TC  $\{100\}$  faces and  $\{111\}$  facets, respectively, excluding the 180 Pt atoms

1  
2  
3  
4 that are on the edges.

5  
6  
7  
8  
9  
10  
11  
12  
13  
14  
15  
16  
17  
18  
19  
20  
21  
22  
23  
24  
25  
26  
27  
28  
29  
30  
31  
32  
33  
34  
35  
36  
37  
38  
39  
40  
41  
42  
43  
44  
45  
46  
47  
48  
49  
50  
51  
52  
53  
54  
55  
56  
57  
58  
59  
60  
Next, we attach octylamine ligands to the surface of the Pt core. The ligand densities and distributions cannot be observed from our TEM measurements, due to the low elemental contrast of molecular ligands. We estimate their local densities by assuming that ligands preferably bind to less coordinated Pt atoms. The coordination numbers for Pt atoms on the {100} faces, edges between two {100} faces, {111} facets, and edges around the {111} facets are 8, 5, 9, and 7, respectively; whereas bulk Pt atoms have the coordination number of 12. In our model, we attach 1 ligand onto each Pt atom on the edges and distribute ligands randomly and evenly on the faces with the density of 2 per 5 Pt atoms. We do not attach ligands on the small corner facets (3 Pt atoms per facet) due to the high steric hindrance between those ligands and ligands that are already attached to the edges. Even though these distributions are rather heuristic, their exact form does not seem to influence much the stability of the self-assembled TCs (see later).

Atomic charges on the (neutral) ligands are based on the CHARMM32 force field.<sup>65</sup> We model the Pt-N charge transfer by adding  $-0.4 e$  to the Pt-bound N atoms of the ligands and  $0.4 e$  to the ligand-hosting Pt atoms. The magnitude of the charge transfer is closely related to the results obtained from *ab initio* studies of  $\text{NH}_x$  species absorbed on Pt surfaces.<sup>62</sup> We keep the rest of the Pt atoms neutral and do not consider the (slight) charge redistribution on the metallic Pt core. If the positive charges on the Pt atoms are left to freely redistribute inside the metallic TC, they would cancel the field in its interior. Their repulsion would cause a slight shift from the area under the ligands toward the corners and lead to the surface charge densities schematically shown in Fig. 6 (a). In our MD simulations, the presence of fixed Pt-N dipoles on the TC faces generates an electric field with the same multipolar symmetry but a smaller strength. When the TCs self-assemble in the *fcc* packing in the experimental system, their charge distribution might be further modified due to the rearrangement (detachment and reattachment) of ligands. Therefore, it is likely that the self-assembled structures have some tolerance with respect to the exact distribution of ligands and the core charging.

#### *b) Modeling of the NC coupling*

We will simulate these RCs and TCs as described in Methods. First, we search for additional local minima in  $\Delta G$  that can help to stabilize the self-assembled superstructures. As discussed above, the vdW ligand-ligand coupling should be relatively small in solvent

(toluene) which is similar to the ligands. Therefore, the additional minima can potentially originate from the Coulombic coupling between the NCs.

During the MD simulations, we keep two adjacent NCs aligned and shifted with respect to each other in vacuum (to simulate a smaller number of atoms) and evaluate their corner-to-corner coupling. We mainly focus on their Coulombic coupling, which is not much affected by the lack of nonpolar solvent, while the vdW coupling is much stronger in its absence. The NCs are placed in a large cubic unit cell (20 nm in length), with periodic boundary conditions applied (NVT ensemble). This (simulation) unit cell is oriented the same way as the unit cells in the *sc* and *fcc* lattices (see Fig. 1), so that  $a_{fcc}$ ,  $b_{fcc}$ , and  $c_{fcc}$  are distances along the simulation  $x$ ,  $y$ , and  $z$  axes, respectively. The centers of two adjacent NCs in the *sc* lattice are separated by the distance  $d_{NC-NC}$ , whereas those in the *fcc* lattice (inter-layer) are separated in the  $x$ ,  $y$ , and  $z$  directions by about one half of the lattice parameters  $a_{fcc}$ ,  $b_{fcc}$ , and  $c_{fcc}$ , respectively. In the simulations, we vary some of these parameters (while fixing others) to evaluate the NC-binding energy.

In each simulation, we allow the ligands to relax while the NC-core atoms are spatially fixed. We first minimize the system energy for  $\approx 1$  ns and then equilibrate the system for  $\approx 2$  ns at the temperature of  $T = 300$  K. We use the last 1.5 ns of the simulation trajectories to evaluate the average Coulombic and vdW (ligand) coupling energy. When we optimize the binding position of the NCs, we briefly release the core atoms and run longer simulations to allow NC movements. We evaluate non-bonded (Coulombic and vdW) interactions of the TCs by pairwise summations of the coupling energies between atoms of both NCs.

*The TC binding energies:* We first calculate the Coulombic and vdW (ligand) binding energies between two adjacent TCs in the shifted corner-to-corner ( $c - c$ ) and face-to-face ( $f - f$ ) configurations. In Fig. 6 (b), we present the total Coulombic energy for TCs in the  $c - c$  configurations. We plot the potential energy surface as a function of the  $a_{fcc}$  and  $c_{fcc}$  parameters ( $b_{fcc}$  is not defined here), starting from the experimentally observed TC separation of  $a_{fcc} = c_{fcc} = 11.0$  nm. A 3D view of the energy surface is shown in the inset. In the studied range of the lattice parameters, the lowest value of the electrostatic energy,  $E_{elec} \approx -47.0$  kcal/mol, is obtained at the experimental TC separation,  $a_{fcc} = c_{fcc} = 11.0$  nm. If we remove the charges associated with the charge separation along the Pt-N bonds (ligand-NC), we get  $E_{elec} \approx 12.9$  kcal/mol for the same TC separation. These coupling energies are significantly larger than those found above for the bulk vdW coupling. Moreover,

only the coupling between two NC neighbors is (so far) included in the energy.

If we let the ligated TCs to spontaneously stabilize their positions, we find that they go to the point of  $a_{fcc} = 11.4$  nm,  $c_{fcc} = 11.8$  nm (see point in Fig 6 (b)), rather than to the experimental point of  $a_{fcc} = c_{fcc} = 11.0$  nm. This is likely caused by the fact that in the experiment the ligands can migrate on the NC surfaces and be further redistributed upon the lattice formation to minimize the coupling energy.<sup>66</sup> The simulations of these relaxed TCs are only done for 2–3 ns to prevent their rotation. In this stabilization, both enthalpic and entropic contributions are involved in  $\Delta G$ .

To estimate the local stability of the TCs with shifted corners, we calculate the binding energy as their truncated corners “slide” on each other. In Fig. 6 (b), this motion goes along the straight line with the slope of  $-\sqrt{2}$ , which passes through the chosen point of  $a_{fcc} = c_{fcc} = 11.8$  nm. We evaluate  $E_{elec}$  along this line up to the point where the center of the two TC facets are at the closest distance and aligned ( $a_{fcc} = 13.8$  nm,  $c_{fcc} = 9.0$  nm). The lowest Coulombic energy along this line is  $E_{elec} \approx -21.4$  kcal/mol, which is found at the point  $a_{fcc} = 12.6$  nm and  $c_{fcc} = 10.7$  nm. This gives a small energy barrier of  $\Delta E_{elec} \approx 1.6$  kcal/mol that keeps the TC corners shifted. If we consider a free redistribution of the charges in the TCs, the energy barrier will likely be higher.

In Fig. 6 (c), we show the dependence of the total Coulombic and vdW energies in the TC pair, as we shift one TC with respect to the other along the  $y$ -direction. We define  $\delta y_{fcc}$  as the shift from the symmetric position. We choose two  $x$  and  $z$  positions of the TCs,  $a_{fcc} = c_{fcc} = 11.0$  nm (double ring in Fig. 6 (b,c)) and  $a_{fcc} = c_{fcc} = 11.8$  nm (single ring in Fig. 6 (b,c)). As discussed earlier, the vdW energy mostly contributes to the NC stabilization after the removal of solvent (its value is then large, as seen here). We can see that for the experimental distances, the vdW energy has a minimum at  $\delta y_{fcc} = 0$ , while the Coulombic energy minimum is shifted to  $\delta y_{fcc} = 0.6$  nm. This slight asymmetry is caused by the random distribution of ligands on the TCs. At the larger separation (11.8 nm), the energy minima are already at  $\delta y_{fcc} = 0$ .

Upon the removal of the solvent, the vdW energy of the coupled ligands becomes large in the  $f-f$  configuration. The question is if the TCs stay in  $c-c$  configuration or spontaneously switch to the  $f-f$  configuration. In order to do so, the TCs would need to be lifted from the potential energy minimum at  $c_{fcc} = 11.8$  nm (equilibrium distance of the  $c-c$  configuration) to the elevation of  $c_{fcc} = 12.94$  nm (equilibrium distance of the  $f-f$  configuration), to be

1  
2  
3  
4 above the steric (ligand) barrier. This lifting is associated with a Coulombic barrier of  $\approx 14$   
5 kcal/mol, which is not thermally accessible. The barrier is about 3 times larger if done from  
6 the experimentally observed height of  $c_{fcc} = 11.0$  nm. In Fig. 6 (d), we fix the TC height  
7 to  $c_{fcc} = 12.94$  nm, and show the Coulombic and vdW energies as the TCs slide on their  
8 faces. The variation of the Coulombic energy is very small, but the vdW energy has a deep  
9 minimum at  $a_{fcc} = 0$  nm ( $f - f$  configuration). We also show by dashed line the partial  
10 dependence of these energies calculated for the experimental TC height of  $c_{fcc} = 11$  nm  
11 (ligand repulsion prevents completion).  
12  
13  
14  
15  
16

17 *Comparison of the TC and RC binding energies:* In Fig. 7, we compare the Coulombic  
18 and vdW (ligand) coupling energies of TCs (left) and RCs (right) in the  $c - c$  (top) and  $f - f$   
19 (bottom) configurations. These energies are calculated as a function of the center-to-center  
20 distance of two (nearest) NCs with fixed cores, where  $a_{fcc} = c_{fcc}$  and  $\delta y_{fcc} = 0$ .  
21  
22  
23

24 First, we consider the  $c - c$  configurations (Fig. 6 (a,b)). If we align both the RCs and  
25 TCs in a similar way,  $d_{NC-NC}$  in TCs is by  $\approx 1$  nm smaller than in RCs, due to the smaller  
26 sizes of their cores ( $l_{TC} = 4.7$  nm and  $l_{RC} = 5.1$  nm). If the NC cores are free to move,  
27 the (relaxed) TCs tend to stabilize in the  $c - c$  configuration (the dark point in Fig. 6 (b))  
28 at  $a_{fcc} = 11.4$  nm and  $c_{fcc} = 11.8$  nm), shown by the vertical line in Fig. 7 (a), while RCs  
29 continue to slide to the  $f - f$  configuration. In the  $c - c$  configuration the Coulombic coupling  
30 energy (relevant in solution) is negative and larger for TCs, while in the  $f - f$  configurations  
31 it is positive and larger for TCs (Fig. 6 (c,d)). Both NCs in vacuum can stabilize in the  
32  $f - f$  configuration; their equilibrium  $d_{NC-NC}$  are shown by the vertical lines in Fig. 6 (c,d).  
33  
34  
35  
36  
37  
38

39 If we compare the vdW (ligand) energies in vacuum for both configurations, we can see  
40 that the  $f - f$  configuration is globally more stable for both RCs and TCs. In the solvent,  
41 the vdW coupling should be small, and the ligands might even cause repulsion between the  
42 NPs.<sup>67</sup> Therefore, it is the Coulombic coupling (together with the bulk vdW coupling) that  
43 can guide and stabilize the loose  $fcc$  structure of TCs.  
44  
45  
46  
47

## 48 Conclusions

49 In summary, we have prepared  $sc$  and  $fcc$  superlattices of ligated regular and truncated  
50 Pt nanocubes, respectively, and used microscopic and atomistic modeling to explain the  
51 remarkably different observed structures. Our results indicate that the  $fcc$  packing can be  
52 stabilized by Coulombic coupling between multipolar electrostatic fields of charged TCs,  
53 which originate from the charge transfer between their ligands and platinum cores. This  
54  
55  
56  
57  
58  
59  
60

1  
2  
3  
4 coupling creates a local energy minimum when the TCs have adjacent (shifted) corners,  
5 which can retain the *fcc* packing in solvent and vacuum against global stabilization of the  
6 *sc* structure. These results could be used in guiding the experimental preparation of novel  
7 supercrystals with many potential applications.  
8  
9

## 10 11 **Methods**

12 We simulate the pairs of RCs and TCs by atomistic molecular dynamics simulations,  
13 using NAMD<sup>68,69</sup> and the CHARMM32 force field.<sup>65</sup> During our simulations, we keep the  
14 temperature fixed by the Langevin dynamics with the damping constant of  $\gamma_{Lang} = 1 \text{ ps}^{-1}$ .  
15 The non-bonded interaction switching distance is set to 8 Å and the cutoff is set to 10  
16 Å. The systems are simulated as NVT ensembles, where the Particle Mesh Ewald (PME)  
17 summation<sup>70</sup> is considered for the Coulombic coupling.  
18  
19  
20  
21

## 22 23 **Acknowledgment.**

24 The authors would like to express their gratitude to Cédric Leuvrey, IPCMS, UMR 7504  
25 CNRS/UdS, Strasbourg, France, for his assistance with the characterization of supercrys-  
26 tals using SEM-FEG, and Pascale Launois and Pierre-Antoine Albouy, LPS, UMR 8502  
27 CNRS/Université Paris Sud, Orsay, France, for their valuable discussions. LV acknowledges  
28 support from UIC Dean Scholar Award. The presented calculations have been partly realized  
29 on the NERSC and NCSA supercomputer networks.  
30  
31  
32  
33  
34

- 
- 35  
36  
37  
38 1. Murray, C. B.; Sun, S.; Doyle, H.; Betley, T. Monodisperse 3d Transition-Metal (Co, Ni,  
39 Fe) Nanoparticles and Their Assembly into Nanoparticle Superlattices. *Mater. Res. Soc. Bull.*  
40 **2001**, *26*, 985–991.  
41
  - 42  
43 2. Alivisatos, A. P. Semiconductor Clusters, Nanocrystals, and Quantum Dots. *Science* **1996**,  
44 *271*, 933–937.  
45
  - 46  
47 3. Buck, M. R.; Bondi, J. F.; Schaak, R. E. A Total-synthesis Framework for The Construction  
48 of High-Order Colloidal Hybrid Nanoparticles. *Nat Chem* **2012**, *4*, 37–44.  
49
  - 50  
51 4. Dong, A.; Ye, X.; Chen, J.; Murray, C. B. Two-Dimensional Binary and Ternary Nanocrystal  
52 Superlattices: The Case of Monolayers and Bilayers. *Nano Lett.* **2011**, *11*, 1804–1809.  
53
  - 54  
55 5. Chang, C.-C.; Wu, H.-L.; Kuo, C.-H.; Huang, M. H. Hydrothermal Synthesis of Monodispersed  
56 Octahedral Gold Nanocrystals with Five Different Size Ranges and Their Self-Assembled Struc-  
57  
58  
59  
60

- 1  
2  
3  
4 tures. *Chem. Mater.* **2008**, *20*, 7570–7574.
- 5  
6 6. Manna, L.; Scher, E. C.; Alivisatos, A. P. Synthesis of Soluble and Processable Rod-, Arrow-,  
7 Teardrop-, and Tetrapod-Shaped CdSe Nanocrystals. *J. Am. Chem. Soc.* **2000**, *122*, 12700–  
8 12706.
- 9  
10  
11 7. Peng, X.; Manna, L.; Yang, W.; Wickham, J.; Scher, E.; Kadavanich, A.; Alivisatos, A. P.  
12 Shape Control of CdSe Nanocrystals. *Nature* **2000**, *404*, 59–61.
- 13  
14 8. Puentes, V. F.; Zanchet, D.; Erdonmez, C. K.; Alivisatos, A. P. Synthesis of hcp-Co Nanodisks.  
15 *J. Am. Chem. Soc.* **2002**, *124*, 12874–12880.
- 16  
17  
18 9. Jun, Y.-W.; Casula, M. F.; Sim, J.-H.; Kim, S. Y.; Cheon, J.; Alivisatos, A. P. Surfactant-  
19 Assisted Elimination of a High Energy Facet as a Means of Controlling the Shapes of TiO<sub>2</sub>  
20 Nanocrystals. *J. Am. Chem. Soc.* **2003**, *125*, 15981–15985.
- 21  
22  
23 10. Wang, Z. L. Transmission Electron Microscopy of Shape-Controlled Nanocrystals and Their  
24 Assemblies. *J. Phys. Chem. B* **2000**, *104*, 1153–1175.
- 25  
26  
27 11. Tao, A. R.; Ceperley, D. P.; Sinsermuksamakul, P.; Neureuther, A. R.; Yang, P. Self-Organized  
28 Silver Nanoparticles for Three-Dimensional Plasmonic Crystals. *Nano Lett.* **2008**, *8*, 4033–  
29 4038.
- 30  
31  
32 12. Glotzer, S. C.; Solomon, M. J. Anisotropy of Building Blocks and Their Assembly into Complex  
33 Structures. *Nat. Mater.* **2007**, *6*, 557–562.
- 34  
35  
36 13. Demortière, A.; Launois, P.; Goubet, N.; Albouy, P.-A.; Petit, C. Shape-Controlled Platinum  
37 Nanocubes and Their Assembly into Two-Dimensional and Three-Dimensional Superlattices.  
38 *J. Phys. Chem. B* **2008**, *112*, 14583–14592.
- 39  
40  
41 14. Lu, W.; Liu, Q.; Sun, Z.; He, J.; Ezeolu, C.; Fang, J. Super Crystal Structures of Octahedral  
42 c-In<sub>2</sub>O<sub>3</sub> Nanocrystals. *J. Am. Chem. Soc.* **2008**, *130*, 6983–6991.
- 43  
44  
45 15. Zheng, R. K.; Gu, H.; Xu, B.; Fung, K. K.; Zhang, X. X.; Ringer, S. P. Self-Assembly and Self-  
46 Orientation of Truncated Octahedral Magnetite Nanocrystals. *Adv. Mater.* **2006**, *18*, 2418–  
47 2421.
- 48  
49  
50 16. Quan, Z.; Fang, J. Superlattices with Non-Spherical Building Blocks. *Nano Today* **2010**, *5*,  
51 390–411.
- 52  
53  
54 17. Murray, C. B.; Kagan, C. R.; Bawendi, M. G. Self-Organization of CdSe Nanocrystallites into  
55 Three-Dimensional Quantum Dot Superlattices. *Science* **1995**, *270*, 1335–1338.
- 56  
57  
58 18. Kovalenko, M. V.; Scheele, M.; Talapin, D. V. Colloidal Nanocrystals with Molecular Metal  
59  
60



- 1  
2  
3  
4 Chalcogenide Surface Ligands. *Science* **2009**, *324*, 1417–1420.
- 5  
6 19. Martin, J. E.; Wilcoxon, J. P.; Odinek, J.; Provencio, P. Control of the Interparticle Spacing  
7 in Gold Nanoparticle Superlattices. *J. Phys. Chem. B* **2000**, *104*, 9475–9486.
- 8  
9 20. Demortière, A.; Buathong, S.; Pichon, B. P.; Panissod, P.; Guillon, D.; Bégin-Colin, S.; Donnio,  
10 B. Nematic-like Organization of Magnetic Mesogen-Hybridized Nanoparticles. *Small* **2010**, *6*,  
11 1341–1346.
- 12  
13 21. Murray, C. B.; Kagan, C. R.; Bawendi, M. G. Synthesis and Characterization of Monodisperse  
14 Nanocrystals and Close-Packed Nanocrystal Assemblies. *Annu. Rev. Mater. Sci.* **2000**, *30*,  
15 545–610.
- 16  
17 22. Puntès, V. F.; Krishnan, K. M.; Alivisatos, A. P. Colloidal Nanocrystal Shape and Size Control:  
18 The Case of Cobalt. *Science* **2001**, *291*, 2115–2117.
- 19  
20 23. Burda, C.; Chen, X.; Narayanan, R.; El-Sayed, M. A. Chemistry and Properties of Nanocrystal  
21 of Different Shapes. *Chem. Rev.* **2005**, *105*, 1025–1102.
- 22  
23 24. Motte, L.; Billoudet, F.; Pileni, M. P. Self-Assembled Monolayer of Nanosized Particles Dif-  
24 fering by Their Sizes. *J. Phys. Chem.* **1995**, *99*, 16425–16429.
- 25  
26 25. Choi, J. J.; Bealing, C. R.; Bian, K.; Hughes, K. J.; Zhang, W.; Smilgies, D.-M.; Hennig,  
27 R. G.; Engstrom, J. R.; Hanrath, T. Controlling Nanocrystal Superlattice Symmetry and  
28 Shape-Anisotropic Interactions through Variable Ligand Surface Coverage. *J. Am. Chem. Soc.*  
29 **2011**, *133*, 3131–3138.
- 30  
31 26. Park, J.; Kang, E.; Son, S.; Park, H.; Lee, M.; Kim, J.; Kim, K.; Noh, H.-J.; Park, J.-H.;  
32 Bae, C.; *et al.* Monodisperse Nanoparticles of Ni and NiO: Synthesis, Characterization, Self-  
33 assembled Superlattices, and Catalytic Applications in the Suzuki Coupling Reaction. *Adv.*  
34 *Mater.* **2005**, *17*, 429–434.
- 35  
36 27. Bell, A. T. The Impact of Nanoscience on Heterogeneous Catalysis. *Science* **2003**, *299*, 1688–  
37 1691.
- 38  
39 28. Mueggenburg, K. E.; Lin, X.-M.; Goldsmith, R. H.; Jaeger, H. M. Elastic Membranes of  
40 Close-packed Nanoparticle Arrays. *Nat. Mater.* **2007**, *6*, 656–660.
- 41  
42 29. Chen, C.-F.; Tzeng, S.-D.; Chen, H.-Y.; Lin, K.-J.; Gwo, S. Tunable Plasmonic Response from  
43 Alkanethiolate-stabilized Gold Nanoparticle Superlattices: Evidence of Near-Field Coupling.  
44 *J. Am. Chem. Soc.* **2007**, *130*, 824–826.
- 45  
46 30. Andres, R. P.; Bielefeld, J. D.; Henderson, J. I.; Janes, D. B.; Kolagunta, V. R.; Kubiak,  
47  
48  
49  
50  
51  
52  
53  
54  
55  
56  
57  
58  
59  
60

- C. P.; Mahoney, W. J.; Osifchin, R. G. Self-Assembly of a Two-Dimensional Superlattice of Molecularly Linked Metal Clusters. *Science* **1996**, *273*, 1690–1693.
31. Zaitseva, N.; Dai, Z. R.; Leon, F. R.; Krol, D. Optical Properties of CdSe Superlattices. *J. Am. Chem. Soc.* **2005**, *127*, 10221–10226.
32. Grzelczak, M.; Mezzasalma, S. A.; Ni, W.; Herasimenka, Y.; Feruglio, L.; Montini, T.; Pérez-Juste, J.; Fornasiero, P.; Prato, M.; Liz-Marzán, L. M. Antibonding Plasmon Modes in Colloidal Gold Nanorod Clusters. *Langmuir* **2011**, ASAP.
33. Ahniyaz, A.; Sakamoto, Y.; Bergström, L. Magnetic Field-induced Assembly of Oriented Superlattices from Maghemite Nanocubes. *PNAS* **2007**, *104*, 17570–17574.
34. Huang, H.-T.; Zhang, B.-T.; He, J.-L.; Yang, J.-F.; Xu, J.-L.; Yang, X.-Q.; Zuo, C.-H.; Zhao, S. Diode-pumped Passively Q-switched Nd:Gd<sub>0.5</sub>Y<sub>0.5</sub>VO<sub>4</sub> Laser at 1.34 $\mu$ m with V<sup>3+</sup>: YAG as the Saturable Absorber. *Opt. Express* **2009**, *17*, 6946–6951.
35. Chen, J.; Lim, B.; Lee, E. P.; Xia, Y. Shape-controlled Synthesis of Platinum Nanocrystals for Catalytic and Electrocatalytic Applications. *Nano Today* **2009**, *4*, 81–95.
36. Bishop, K. J. M.; Wilmer, C. E.; Soh, S.; Grzybowski, B. A. Nanoscale Forces and Their Uses in Self-Assembly. *Small* **2009**, *5*, 1600–1630.
37. Nie, Z.; Fava, D.; Kumacheva, E.; Zou, S.; Walker, G. C.; Rubinstein, M. Self-Assembly of Metal-Polymer Analogues of Amphiphilic Triblock Copolymers. *Nat Mater* **2007**, *6*, 609–614.
38. Korgel, B. A.; Fullam, S.; Connolly, S.; Fitzmaurice, D. Assembly and Self-Organization of Silver Nanocrystal Superlattices: Ordered “Soft Spheres”. *J. Phys. Chem. B* **1998**, *102*, 8379–8388.
39. Grzelczak, M.; Vermant, J.; Furst, E. M.; Liz-Marzán, L. M. Directed Self-Assembly of Nanoparticles. *ACS Nano* **2010**, *4*, 3591–3605.
40. Bodnarchuk, M. I.; Kovalenko, M. V.; Heiss, W.; Talapin, D. V. Energetic and Entropic Contributions to Self-Assembly of Binary Nanocrystal Superlattices: Temperature as the Structure-directing Factor. *J. Am. Chem. Soc.* **2010**, *132*, 11967–11977.
41. Min, Y.; Akbulut, M.; Kristiansen, K.; Golan, Y.; Israelachvili, J. The Role of Interparticle and External Forces in Nanoparticle Assembly. *Nat. Mater.* **2008**, *7*, 527–538.
42. Talapin, D. V.; Shevchenko, E. V.; Murray, C. B.; Titov, A. V.; Král, P. Dipole-Dipole Interactions in Nanoparticle Superlattices. *Nano Lett.* **2007**, *7*, 1213–1219.
43. Titov, A. V.; Král, P. Modeling the Self-Assembly of Colloidal Nanorod Superlattices. *Nano*

- 1  
2  
3  
4 *Lett.* **2008**, *8*, 3605–3612.
- 5  
6 44. Clancy, P. Nanoparticles: Self-Assembly Finds Its Own Limits. *Nat Nano* **2011**, *6*, 540–541.
- 7  
8 45. Henry, A.-I.; Courty, A.; Pileni, M.-P.; Albouy, P.-A.; Israelachvili, J. Tuning of Solid Phase  
9 in Supracrystals Made of Silver Nanocrystals. *Nano Lett.* **2008**, *8*, 2000–2005.
- 10  
11 46. He, J.; Lin, X.-M.; Chan, H.; Vuković, L.; Král, P.; Jaeger, H. M. Diffusion and Filtration  
12 Properties of Self-Assembled Gold Nanocrystal Membranes. *Nano Lett.* **2011**, *11*, 2430–2435.
- 13  
14 47. Chan, H.; Král, P. Self-standing Nanoparticle Membranes and Capsules, *Nanoscale* **2011**, *3*,  
15 1881–1886.
- 16  
17 48. Shevchenko, E. V.; Talapin, D. V.; Kotov, N. A.; O'Brien, S.; Murray, C. B. Structural  
18 Diversity in Binary Nanoparticle Superlattices. *Nature* **2006**, *439*, 55–59.
- 19  
20 49. Ohara, P. C.; Leff, D. V.; Heath, J. R.; Gelbart, W. M. Crystallization of Opals from Polydis-  
21 perse Nanoparticles. *Phys. Rev. Lett.* **1995**, *75*, 3466–3469.
- 22  
23 50. Chen, Z.; Moore, J.; Radtke, G.; Siringhaus, H.; O'Brien, S. Binary Nanoparticle Superlattices  
24 in the Semiconductor-Semiconductor System: CdTe and CdSe. *J. Am. Chem. Soc.* **2007**, *129*,  
25 15702–15709.
- 26  
27 51. Yamamuro, S.; Sumiyama, K.; Kamiyama, T. Shape-induced Simple Cubic Arrangement in  
28 Three-Dimensional Nanocube Self-Assemblies. *Appl. Phys. Lett.* **2008**, *92*, 113108.
- 29  
30 52. Stoeva, S. I.; Prasad, B. L. V.; Uma, S.; Stoimenov, P. K.; Zaikovski, V.; Sorensen, C. M.;  
31 Klabunde, K. J. Face-Centered Cubic and Hexagonal Closed-Packed Nanocrystal Superlattices  
32 of Gold Nanoparticles Prepared by Different Methods. *J. Phys. Chem. B* **2003**, *107*, 7441–  
33 7448.
- 34  
35 53. Stebe, K. J.; Lewandowski, E.; Ghosh, M. Oriented Assembly of Metamaterials. *Science* **2009**,  
36 *325*, 159–160.
- 37  
38 54. Henzie, J.; Grünwald, M.; Widmer-Cooper, A.; Geissler, P. L.; Yang, P. Self-assembly of  
39 Uniform Polyhedral Silver Nanocrystals into Densest Packings and Exotic Superlattices. *Nat*  
40 *Mater* **2011**, DOI: 10.1038/NMAT3178.
- 41  
42 55. Motte, L.; Billoudet, F.; Lacaze, E.; Douin, J.; Pileni, M. P. Self-Organization into 2D and  
43 3D Superlattices of Nanosized Particles Differing by Their Size. *J. Phys. Chem. B* **1997**, *101*,  
44 138–144.
- 45  
46 56. Demortière, A.; Petit, C. First Synthesis by Liquid-Liquid Phase Transfer of Magnetic  
47  $\text{Co}_x\text{Pt}_{100-x}$  Nanoalloys. *Langmuir* **2007**, *23*, 8575–8584.
- 48  
49  
50  
51  
52  
53  
54  
55  
56  
57  
58  
59  
60

- 1  
2  
3  
4 57. Kraig, R. E.; Roundy, D.; Cohen, M. L. A Study of the Mechanical and Structural Properties  
5 of Polonium. *Solid State Communications* **2004**, *129*, 411–413.
- 6  
7 58. Li, F.; Delo, S. A.; Stein, A. Disassembly and Self-Reassembly in Periodic Nanostructures: A  
8 Face-Centered-to-Simple-Cubic Transformation. *Angew. Chem., int. Ed.* **2007**, *46*, 6666–6669.
- 9  
10 59. Yamamuro, S.; Sumiyama, K. Why Do Cubic Nanoparticles Favor a Square Array? Mecha-  
11 nism of Shape-Dependent Arrangement in Nanocube Self-Assemblies. *Chemical Physics Letters*  
12 **2006**, *418*, 166–169.
- 13  
14 60. Yao, H.; Minami, T.; Hori, A.; Koma, M.; Kimura, K. Fivefold Symmetry in Superlattices of  
15 Monolayer-Protected Gold Nanoparticles. *J. Phys. Chem. B* **2006**, *110*, 14040–14045.
- 16  
17 61. Cölfen, H.; Mann, S. Higher-Order Organization by Mesoscale Self-Assembly and Transforma-  
18 tion of Hybrid Nanostructures. *Angew. Chem., int. Ed.* **2003**, *42*, 2350–2365.
- 19  
20 62. Novell-Leruth, G.; Valcárcel, A.; Clotet, A.; Ricart, J. M.; Pérez-Ramírez, J. DFT Character-  
21 ization of Adsorbed NH<sub>x</sub> Species on Pt(100) and Pt(111) Surfaces. *J. Phys. Chem. B* **2005**,  
22 *109*, 18061–18069.
- 23  
24 63. Hamaker, H.C. The London - Van der Waals Attraction between Spherical Particles. *Physica*  
25 **1937**, *4*, 1058–1072.
- 26  
27 64. Luedtke, W. D.; Landman, U. Structure, Dynamics, and Thermodynamics of Passivated Gold  
28 Nanocrystallites and Their Assemblies. *J. Phys. Chem.* **1996**, *100*, 13323–13329.
- 29  
30 65. MacKerell, A. D.; Bashford, D.; Bellott, M.; Dunbrack, R. L.; Evanseck, J. D.; Field, M. J.;  
31 Fischer, S.; Gao, J.; Guo, H.; Ha, S.; *et al.* All-Atom Empirical Potential for Molecular Mod-  
32 eling and Dynamics Studies of Proteins. *J. Phys. Chem. B* **1998**, *102*, 3586–3616.
- 33  
34 66. Ionita, P.; Volkov, A.; Jeschke, G.; Chechik, V. Lateral Diffusion of Thiol Ligands on the  
35 Surface of Au Nanoparticles: An Electron Paramagnetic Resonance Study. *Anal. Chem.* **2007**,  
36 *80*, 95–106.
- 37  
38 67. Schapotschnikow, P.; Pool, R.; Vlugt, T. J. H. Molecular Simulations of Interacting Nanocrys-  
39 tals. *Nano Lett.* **2008**, *8*, 2930–2934.
- 40  
41 68. Phillips, J. C.; Braun, R.; Wang, W.; Gumbart, J.; Tajkhorshid, E.; Villa, E.; Chipot, C.;  
42 Skeel, R. D.; Kalé, L.; Schulten, K. Scalable Molecular Dynamics with NAMD. *J. Comput.*  
43 *Chem.* **2005**, *26*, 1781–1802.
- 44  
45 69. Humphrey, W.; Dalke, A.; Schulten, K. VMD: Visual Molecular Dynamics. *J. Mol. Graphics*  
46 **1996**, *14*, 33–38.
- 47  
48  
49  
50  
51  
52  
53  
54  
55  
56  
57  
58  
59  
60

- 1  
2  
3  
4 70. Darden, T.; York, D.; Pedersen, L. Particle Mesh Eward: An  $N \cdot \log(N)$  Method for Ewald  
5 Sums in Large Systems. *J. Chem. Phys.* **1993**, *98*, 185503.  
6  
7  
8  
9  
10  
11  
12  
13  
14  
15  
16  
17  
18  
19  
20  
21  
22  
23  
24  
25  
26  
27  
28  
29  
30  
31  
32  
33  
34  
35  
36  
37  
38  
39  
40  
41  
42  
43  
44  
45  
46  
47  
48  
49  
50  
51  
52  
53  
54  
55  
56  
57  
58  
59  
60

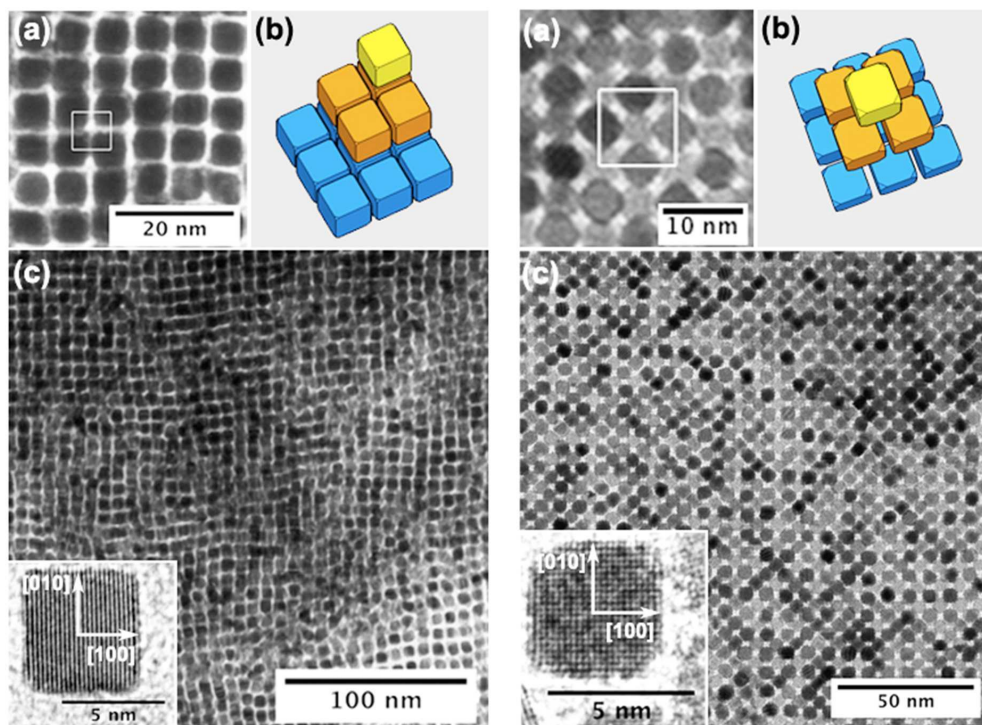


Figure 1: Experimentally observed superstructures of self-assembled regular (RCs) and truncated (TCs) colloidal octylamine-coated platinum nanocubes in toluene: (left) (a) Square array of RCs. (b) Scheme of the simple cubic structure. (c) Multi-layers of organized RCs. (inset) TEM image of a RC. (right) (a) Square array of TCs. (b) Scheme of the *fcc* structure. (c) Multi-layers of organized TCs. (inset) TEM image of a TC.

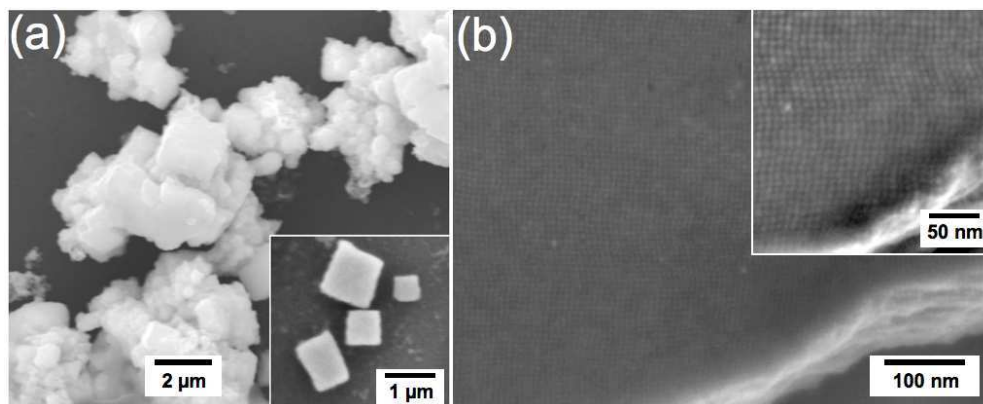


Figure 2: (a) SEM images of stacked *sc* supercrystals of RCs. (inset) Individual RC supercrystals. (b) SEM-FEG images of a RC supercrystal. (inset) Magnified SEM image showing the arrangement of RCs within the supercrystal.

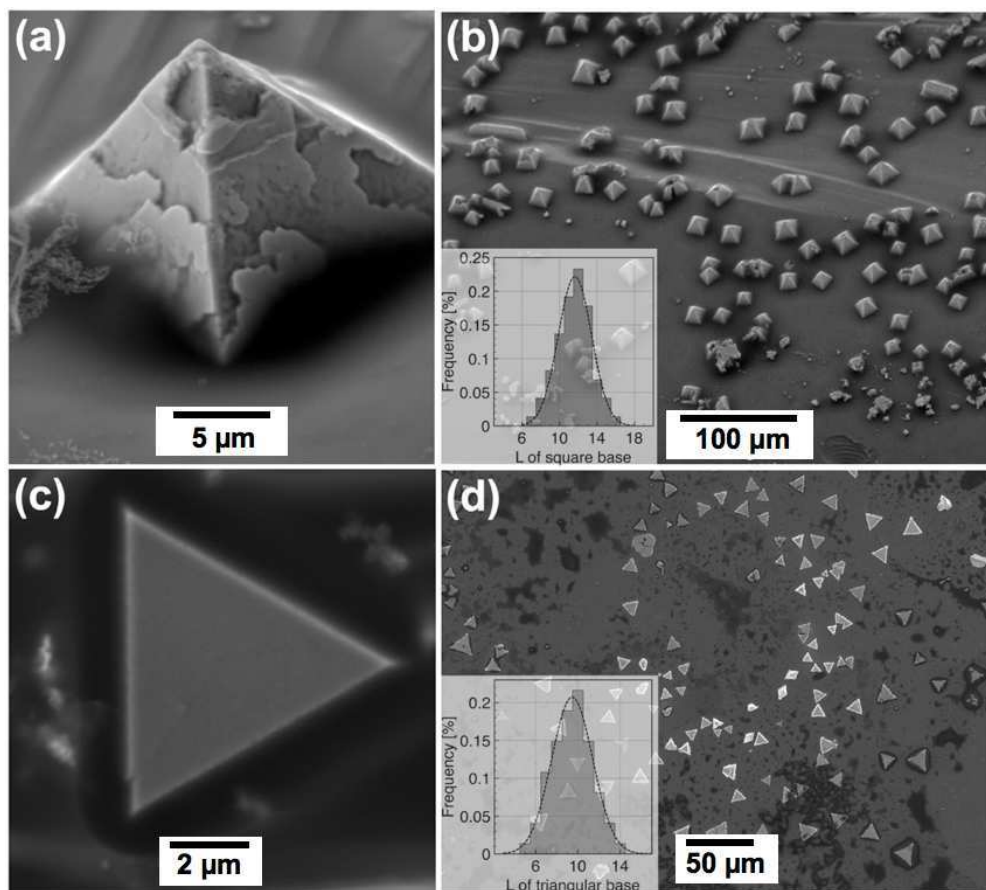


Figure 3: SEM images of *fcc* supercrystals of TCs. (a) Superlattice of square pyramidal shape. (b) Ensemble of square pyramidal supercrystals and their size distributions (inset). (c) Superlattice of triangular prism shape. (d) Triangular prism supercrystals and their size distribution (inset).



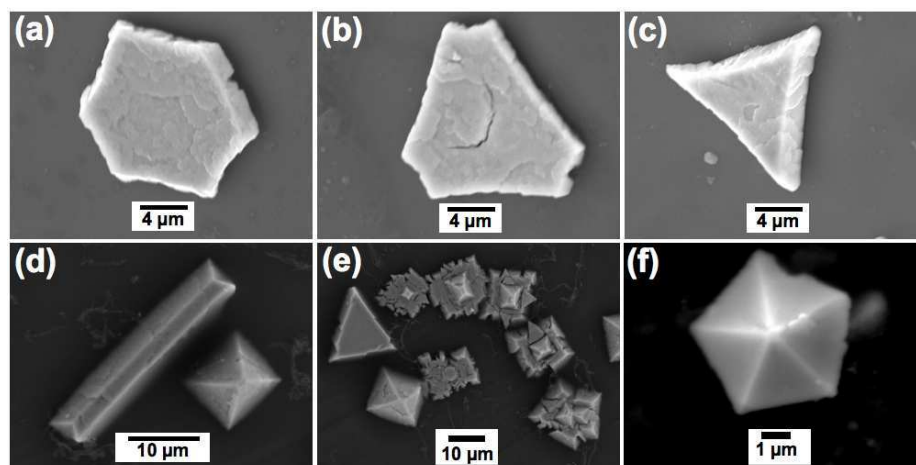


Figure 4: SEM images of TC supercrystals. (a) Hexagonal shape. (b) Quasi hexagonal. (c) Triangular. (d) Elongated. (e) Cleaved (crushed). (f) Decahedral.

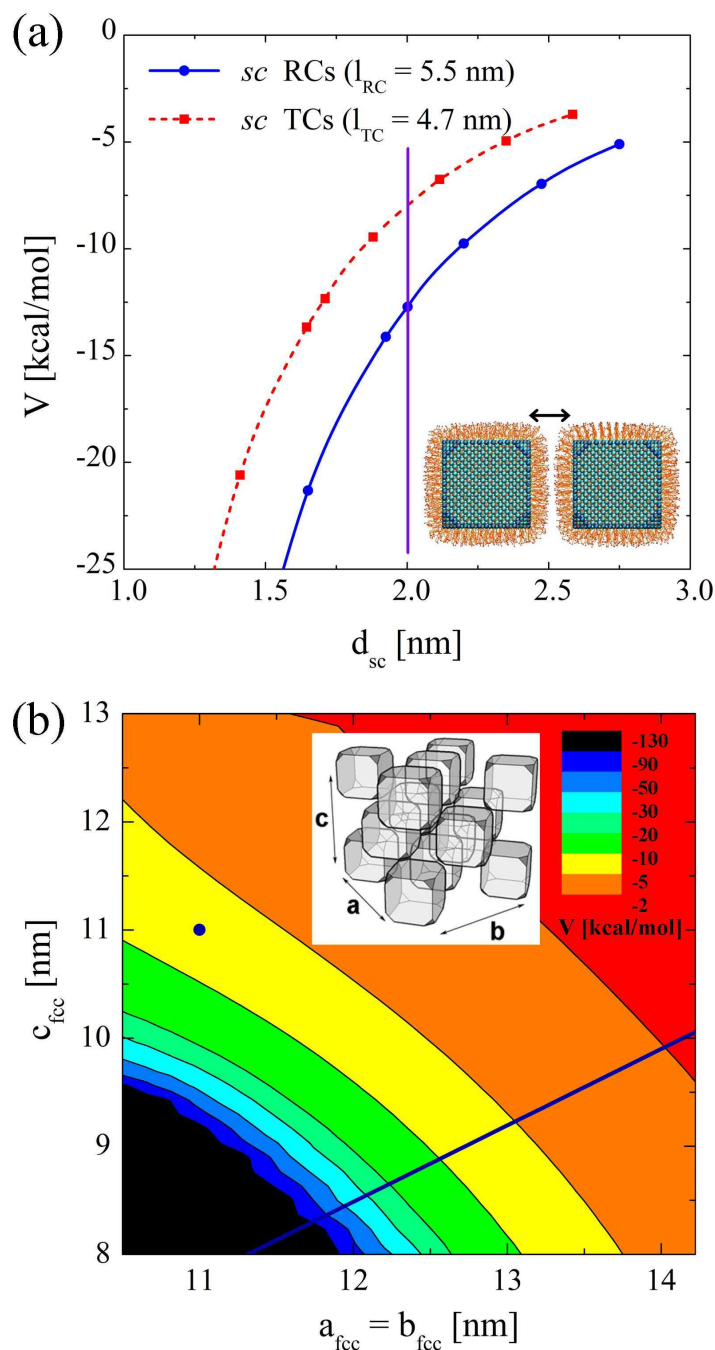


Figure 5: (a) The vdW potential energy per particle for  $sc$  structures,  $V^{sc}$ , of RCs and TCs in dependence on the face-to-face inter-nanocube distance  $d_{sc}$ . The vertical line marks the experimentally observed  $d_{sc}$  for RCs in the  $sc$  superlattice. (b) The vdW potential energy per particle for  $fcc$  structures,  $V^{fcc}$ , of TCs in dependence on the parameters  $a_{fcc} = b_{fcc}$  and  $c_{fcc}$ . The line ( $a_{fcc} = b_{fcc} = \sqrt{2}c_{fcc}$ ) represents parameters for which the TCs have aligned corner facets.

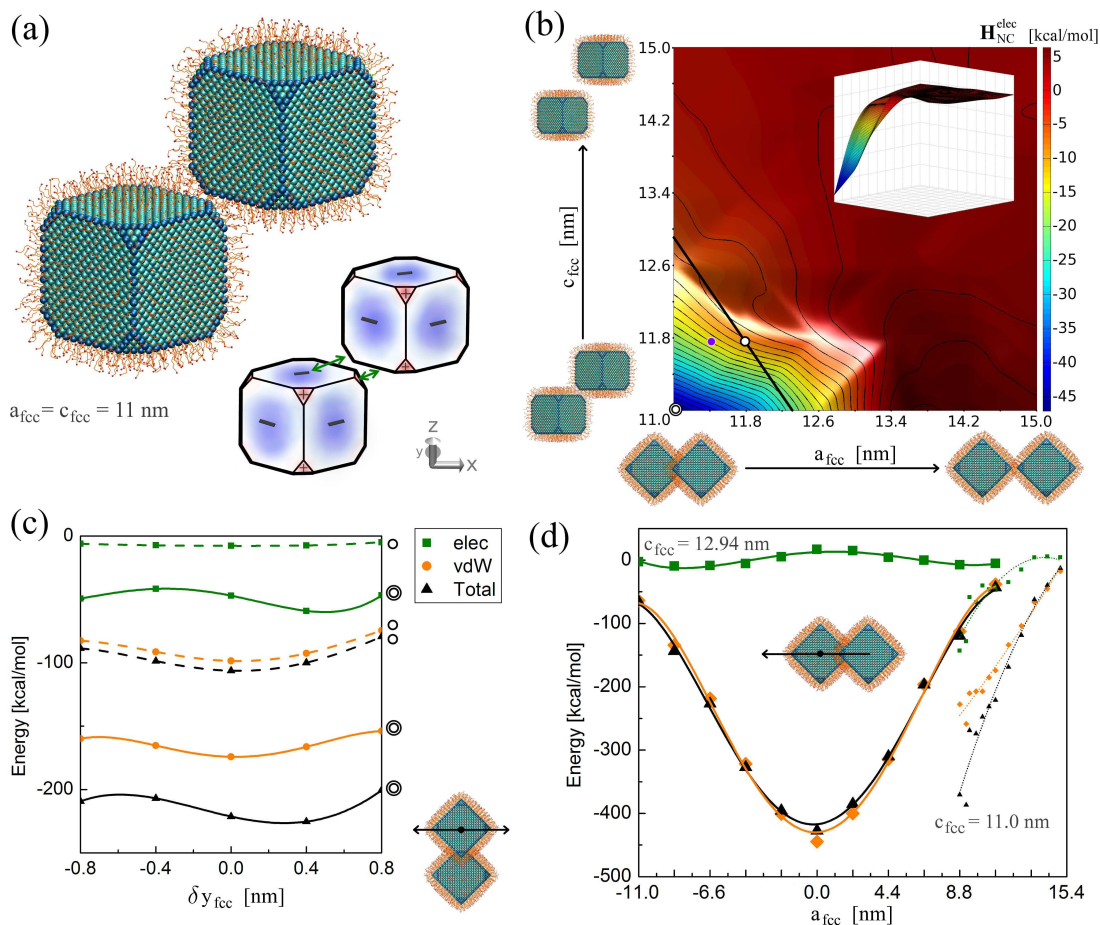


Figure 6: (a) Atomistic model of TCs in the experimentally predicted  $c-c$  configuration, with H atoms hidden. The schematic drawing shows one possible charge distribution on the surface of the TCs that can stabilize the structure through the attractions shown by the arrows. (b) Contour plot of the Coulombic coupling energy of TCs starting from the predicted  $c-c$  configuration. The inset shows a 3D view of the energy surface. (c) Coulombic and vdW (ligand) coupling energies of TCs that are slightly shifted from the  $a_{fcc} = c_{fcc} = 11.0$  nm and  $a_{fcc} = c_{fcc} = 11.8$  nm configurations along the  $y$ -direction. The two configurations are labeled by single ring or double ring icon on the right of each curve. (d) The Coulombic and vdW (ligand) coupling energies of NCs as a function of  $a_{fcc}$  are evaluated to cover the transition from the  $c-c$  configuration to the  $f-f$  configuration at the height of  $c_{fcc} = 12.94$  nm and  $c_{fcc} = 11.0$  nm.

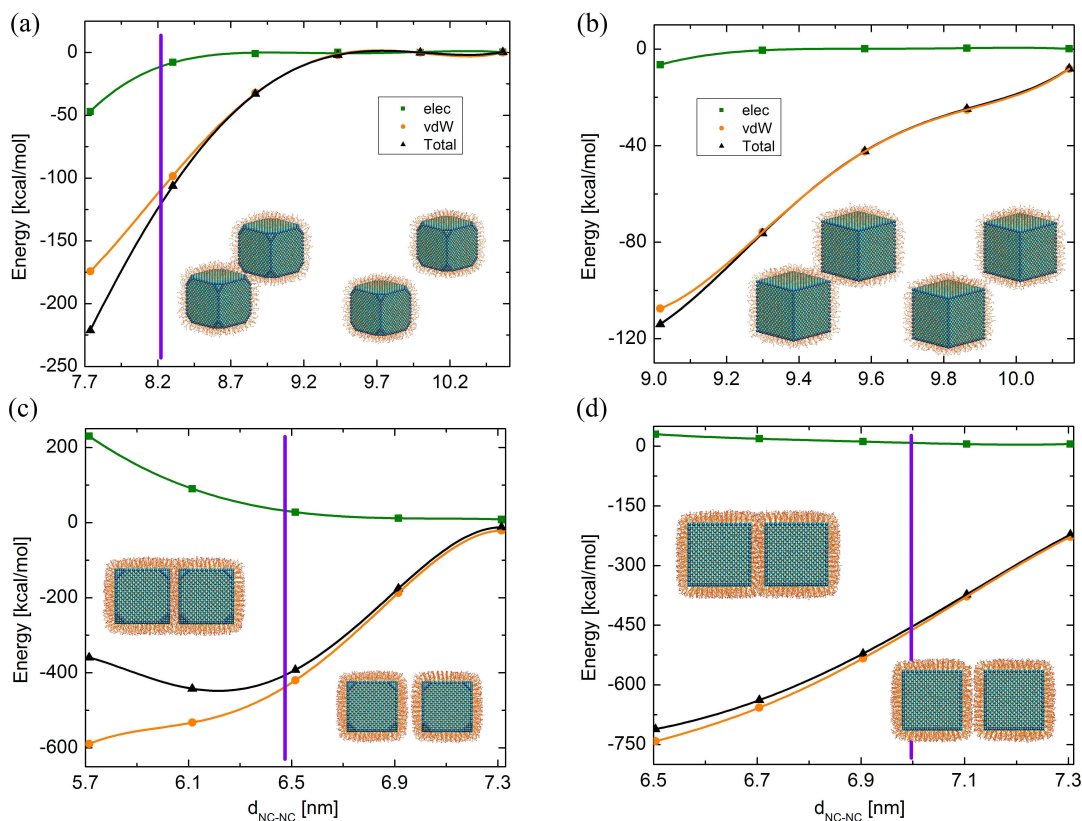
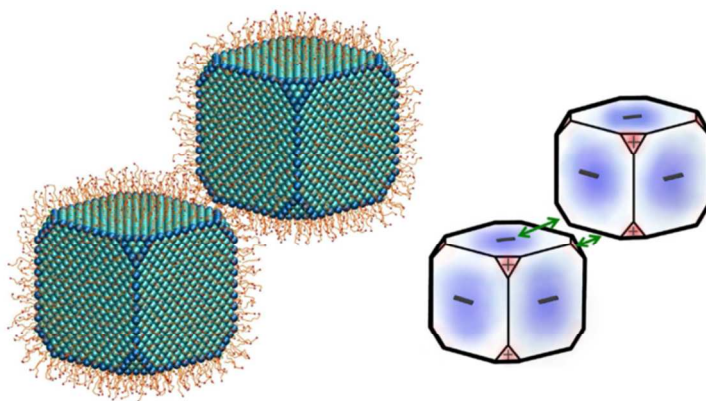
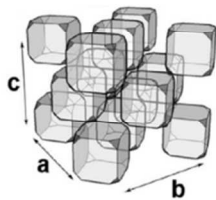
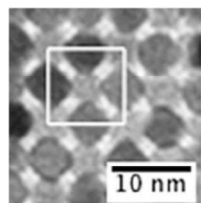


Figure 7: The Coulombic and vdW (ligand) coupling energies of NCs as a function of the (inter-layer) center-to-center inter-nanocube distance,  $d_{NC-NC}$ , for (a) TCs in the  $c-c$  configuration. (b) RCs in the  $c-c$  configuration. (c) TCs in the  $f-f$  configuration. (d) RCs in the  $f-f$  configuration. Schematic drawings in each plot show the configurations of the two end points. The vertical lines show the equilibrated distances of NCs with relaxed cores.

1  
2  
3  
4  
5  
6  
7  
8  
9  
10  
11  
12  
13  
14  
15  
16  
17  
18  
19  
20  
21  
22  
23  
24  
25  
26  
27  
28  
29  
30  
31  
32  
33  
34  
35  
36  
37  
38  
39  
40  
41  
42  
43  
44  
45  
46  
47  
48  
49  
50  
51  
52  
53  
54  
55  
56  
57  
58  
59  
60



81x36mm (300 x 300 DPI)